Collective Rabi dynamics of electromagnetically coupled quantum-dot ensembles

Connor Glosser, B. Shanker, and Carlo Piermarocchi

Collective Rabi dynamics of electromagnetically-coupled quantum dot ensembles

Connor Glosser,[1, 2, ∗] B. Shanker,[2] and Carlo Piermarocchi[1, †]

[1]*Department of Physics & Astronomy, Michigan State University*
567 Wilson Road, East Lansing MI 48824 USA
[2]*Department of Electrical & Computer Engineering, Michigan State University*
428 South Shaw Lane, East Lansing MI 48824, USA
(Dated: August 7, 2017)

Rabi oscillations typify the inherent nonlinearity of optical excitations in quantum dots. Using an integral kernel formulation to solve the 3D Maxwell-Bloch equations in ensembles of up to 10^4 quantum dots, we observe features in Rabi oscillations due to the interplay of nonlinearity, non-equilibrium excitation, and electromagnetic coupling between the dots. This approach allows us to observe the dynamics of each dot in the ensemble without resorting to spatial averages. Our simulations predict synchronized multiplets of dots that exchange energy, dots that dynamically couple to screen the effect of incident external radiation, localization of the polarization due to randomness and interactions, as well as wavelength-scale regions of enhanced and suppressed polarization.

PACS numbers: 1.1

I. INTRODUCTION

Semiconductor structures containing a large number of quantum dots offer ideal environments for exploring collective effects induced by light-matter interactions. Often, these structures exhibit new phenomena due to geometrical randomness and nonlinearities in the underlying system dynamics. Additionally, optical excitations (excitons) undergo characteristic Rabi oscillations [1–3] in quantum dots analogous to those observed in atomic systems; as quantum dots have stronger dipolar transitions than atoms, these light-induced oscillations generate secondary fields that couple the system more strongly than equivalent atomic species. We can therefore expect—at least in some regions of the sample—these local secondary fields will produce modified collective behavior in the exciton dynamics. Phenomena induced by these secondary fields have received considerable theoretical/computational [4, 5] and experimental [6] attention as they may provide new insight on the coherent dynamics of excitons in quantum dot systems.

In the realm of theoretical/computational investigation, researchers in atomic and solid-state optics have developed numerous variations of the Maxwell-Bloch equations [7] to describe features such as ringing in pulse propagation [8, 9] or emission fluctuations [10]. Early solution strategies for these equations fell to continuum models [9, 11] that recover effects arising from far-field interactions or describe near-field phenomena assuming spatial homogeneity [12]. More recently, mesh-based PDE solvers [13–15] added a large degree of fidelity to these models, though the finite size of the mesh means they still have trouble resolving short-range effects without unduly increasing the computational cost. Additionally, the nature of these meshes make them prohibitively expensive

to extend into higher dimensional geometries for optically-large systems. In this work we develop a computational framework to discover signatures of collective effects in strongly-driven quantum dots within a microscopic formalism. By constructing the Maxwell-Bloch equations with an integral kernel to describe radiation, we recover near- and far-electric fields with full fidelity across the simulation while allowing for dynamics at the level of individual quantum dots. Our methodology—based on successful models of other electromagnetic [16–18] and acoustic [19–21] systems—accommodates 10^4 particles distributed over optically-large regions in three dimensions.

As we explicitly track the evolution of each quantum dot in the system, we will numerically demonstrate that the collective Rabi oscillation can induce significant coupling in sufficiently close quantum dots. This laser-induced inter-dot coupling manifests itself in different forms: (i) The polarization generated in isolated quantum dot pairs dynamically suppresses the Rabi rotation. We interpret this as the consequence of a time-dependent energy shift that brings the pair temporarily out of resonance with the external driving field. (ii) In addition to this screening, we observe oscillations in the free-induction decay for larger multiplets of quantum dots. (iii) Optical pulses of integer π area, for which we expect no polarization in uncoupled systems following the pulse, produce patterns of residual localized polarization that remain in the system. (iv) The long-range interactions in optically-large systems produce wavelength-scale regions of enhanced and suppressed polarization. These effects could, for instance, help identify multiplets of dots that dynamically couple during Rabi oscillations, or help understand nonlinear pulse propagation effects in these media.

We structure the remainder of this paper as follows: section II motivates the physical model of an ensemble of two-level systems that interact through a classical electric field. Section III presents the details of our methodology

---

∗ Corresponding author; glosser1@msu.edu
† piermaro@msu.edu

in the context of a global rotating-wave approximation and we offer an implementation of this algorithm at [22]. Section IV contains the results of our investigation where we observe polarization features not present in noninteracting systems at both sub- and super-wavelength scales. Finally, section V contains concluding remarks where we hypothesize on the mechanisms underpinning the observed polarization features as well as comment on our future work in this area.

II. PROBLEM STATEMENT

Consider the evolution of a set of quantum dots in response to a time-varying electric field. If we concern ourselves only with electric dipole transitions in a resonant (or nearly-resonant) system, we may write the time-dependence of a given quantum dot's density matrix, $\hat{\rho}(t)$, as

$$\frac{\mathrm{d}\hat{\rho}}{\mathrm{d}t} = \frac{-i}{\hbar}\left[\hat{\mathcal{H}}(t), \hat{\rho}\right] - \hat{\mathcal{D}}[\hat{\rho}]. \tag{1}$$

Here, $\hat{\mathcal{H}}(t)$ represents a local Hamiltonian that governs the internal two-level structure of the quantum dot, as well as its interaction with an external electromagnetic field, and $\hat{\mathcal{D}}$ provides dissipation terms that account for emission effects phenomenologically. Formally,

$$\hat{\mathcal{H}}(t) \equiv \begin{pmatrix} 0 & \hbar\chi(t) \\ \hbar\chi^*(t) & \hbar\omega_0 \end{pmatrix} \tag{2a}$$

$$\hat{\mathcal{D}}[\hat{\rho}] \equiv \begin{pmatrix} (\rho_{00}-1)/T_1 & \rho_{01}/T_2 \\ \rho_{10}/T_2 & \rho_{11}/T_1 \end{pmatrix} \tag{2b}$$

where $\chi(t) \equiv \mathbf{d} \cdot \hat{\mathbf{E}}(\mathbf{r},t)/\hbar$, $\mathbf{d} \equiv \langle 1|e\hat{\mathbf{r}}|0\rangle$, and $|0\rangle$ & $|1\rangle$ represent the highest valence and lowest conduction states of the quantum dot under consideration. Finally, the T_1 and T_2 constants characterize average emission and relaxation times.

To account for the interactions between quantum dots, we turn to a semiclassical description of the system under the assumption of coherent fields and negligible quantum statistics effects. Such an approximation preserves the discrete two-level energy structure of *individual* quantum dots though electromagnetic quantities behave like their classical analogues. We define the total electric field at any point as $\mathbf{E}(\mathbf{r},t) = \mathbf{E}_L(\mathbf{r},t) + \mathfrak{F}\{\mathbf{P}(\mathbf{r},t)\}$ where

$\mathbf{E}_L(\mathbf{r},t)$ describes an incident laser field, $\mathbf{P}(\mathbf{r},t)$ a polarization distribution arising from the off-diagonal elements (coherences) of $\hat{\rho}$, and

$$\mathfrak{F}\{\mathbf{P}(\mathbf{r},t)\} \equiv \frac{-1}{4\pi\epsilon}\int \left(\overset{\leftrightarrow}{\mathrm{I}} - \bar{\mathbf{r}}\otimes\bar{\mathbf{r}}\right) \cdot \frac{\partial_t^2\mathbf{P}(\mathbf{r}',t_R)}{c^2|\mathbf{r}-\mathbf{r}'|} + \\ \left(\overset{\leftrightarrow}{\mathrm{I}} - 3\bar{\mathbf{r}}\otimes\bar{\mathbf{r}}\right) \cdot \left(\frac{\partial_t\mathbf{P}(\mathbf{r}',t_R)}{c|\mathbf{r}-\mathbf{r}'|^2} + \frac{\mathbf{P}(\mathbf{r}',t_R)}{|\mathbf{r}-\mathbf{r}'|^3}\right)\mathrm{d}^3\mathbf{r}' \tag{3}$$

(see §72 of [23]). Here, $\overset{\leftrightarrow}{\mathrm{I}}$ denotes the identity dyad, $\bar{\mathbf{r}} \equiv (\mathbf{r}-\mathbf{r}')/|\mathbf{r}-\mathbf{r}'|$, $\otimes$ represents the tensor product (i.e. $(\mathbf{a}\otimes\mathbf{b})_{ij} = a_ib_j$), $t_R \equiv t - |\mathbf{r}-\mathbf{r}'|/c$, and ϵ gives the dielectric constant of the inter-dot medium. Thus, in a system composed of multiple quantum dots, eq. (3) couples the evolution of each quantum dot by way of the off-diagonal matrix elements appearing in eq. (2a). Note that this approach does not require an instantaneous dipole-dipole Coulomb term between (charge-neutral) quantum dots; the interactions between structures occur only via the electric field which propagates through space with finite velocity. (See A_{IV} and C_{IV} of [24] for in-depth discussions of this point.)

In the systems under consideration here, ω_0 lies in the optical frequency band ($\sim 1500\,\mathrm{meV}/\hbar$). As such, naïvely integrating eq. (1) to resolve the Rabi dynamics that occur on the order of $1\,\mathrm{ps}$ becomes computationally infeasible. By introducing $\tilde{\rho} = \hat{U}\hat{\rho}\hat{U}^\dagger$ where $\hat{U} = \mathrm{diag}(1, e^{i\omega_L t})$, we may instead write eq. (1) as

$$\frac{\mathrm{d}\tilde{\rho}}{\mathrm{d}t} = \frac{-i}{\hbar}\left[\hat{U}\hat{\mathcal{H}}\hat{U}^\dagger - i\hbar\hat{V}, \tilde{\rho}\right] - \hat{\mathcal{D}}[\tilde{\rho}], \quad \hat{V} \equiv \hat{U}\frac{\mathrm{d}\hat{U}^\dagger}{\mathrm{d}t} \tag{4}$$

which will contain only terms proportional to $e^{i(\omega_0 \pm \omega_L)t}$ if $\mathbf{E}(t) \sim \tilde{\mathbf{E}}(t)\cos(\omega_L t)$. Consequently, we ignore the high-frequency quantities under the assumption that such terms will integrate to zero in solving eq. (4) over appreciable timescales [25]. As the system no longer contains any optical frequencies, one can then construct efficient numerical strategies for solving eq. (4).

Due to the quantum mechanical transitions at play in producing secondary radiation, we may assume similarly monochromatic radiated fields. As such, a similar transformation applies to the source distribution in eq. (3). Writing $\mathbf{P}(\mathbf{r},t) = \tilde{\mathbf{P}}(\mathbf{r},t)e^{i\omega_L t}$ and similarly ignoring high-frequency terms, the radiated field envelope becomes

$$\tilde{\mathfrak{F}}\{\tilde{\mathbf{P}}(\mathbf{r},t)\} \equiv \frac{-1}{4\pi\varepsilon}\int \left(\overset{\leftrightarrow}{\mathrm{I}} - \bar{\mathbf{r}}\otimes\bar{\mathbf{r}}\right) \cdot \frac{\left(\partial_t^2\tilde{\mathbf{P}}(\mathbf{r}',t_R) + 2i\omega_L\partial_t\tilde{\mathbf{P}}(\mathbf{r}',t_R) - \omega_L^2\tilde{\mathbf{P}}(\mathbf{r}',t_R)\right)e^{-i\omega_L|\mathbf{r}-\mathbf{r}'|/c}}{c^2|\mathbf{r}-\mathbf{r}'|} + \\ \left(\overset{\leftrightarrow}{\mathrm{I}} - 3\bar{\mathbf{r}}\otimes\bar{\mathbf{r}}\right) \cdot \frac{\left(\partial_t\tilde{\mathbf{P}}(\mathbf{r}',t_R) + i\omega_L\tilde{\mathbf{P}}(\mathbf{r}',t_R)\right)e^{-i\omega_L|\mathbf{r}-\mathbf{r}'|/c}}{c|\mathbf{r}-\mathbf{r}'|^2} + \left(\overset{\leftrightarrow}{\mathrm{I}} - 3\bar{\mathbf{r}}\otimes\bar{\mathbf{r}}\right) \cdot \frac{\tilde{\mathbf{P}}(\mathbf{r}',t_R)e^{-i\omega_L|\mathbf{r}-\mathbf{r}'|/c}}{|\mathbf{r}-\mathbf{r}'|^3}\,\mathrm{d}^3\mathbf{r}'. \tag{5}$$

Critically, eq. (5) maintains the high-frequency phase relationship between sources oscillating at ω_L via the
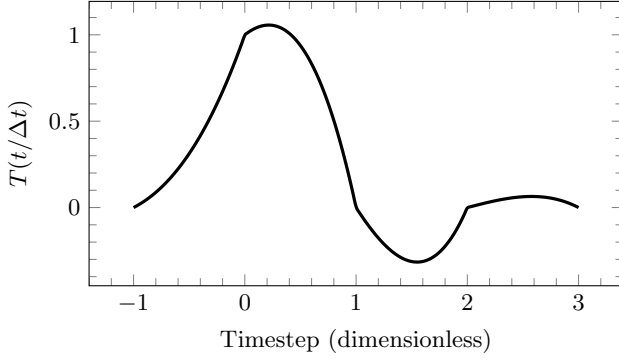
FIG. 1. Nonorthogonal and C^0-continuous temporal basis function $T(t/\Delta t)$ constructed from intervals of third-order Lagrange polynomials.

factors of $e^{-i\omega_L|\mathbf{r}-\mathbf{r}'|/c}$ that appear.

III. COMPUTATIONAL APPROACH

To solve eqs. (4) and (5) for each of N_s quantum dots at N_t equally-spaced timesteps, we begin with a suitable representation of $\tilde{\mathbf{P}}(\mathbf{r}, t)$ in terms of spatial and temporal basis functions, i.e.

$$\tilde{\mathbf{P}}(\mathbf{r}, t) = \sum_{\ell=0}^{N_s-1} \sum_{m=0}^{N_t-1} \mathcal{A}_\ell^{(m)} \mathbf{S}_\ell(\mathbf{r}) T(t - m\,\Delta t). \qquad (6)$$

As the wavelength of any radiation in the system far exceeds the dimensions of the quantum dots under consideration, we take $\mathbf{S}_\ell(\mathbf{r}) \equiv \mathbf{d}_\ell \delta(\mathbf{r} - \mathbf{r}_\ell)$ where $\mathbf{d}_\ell$ and $\mathbf{r}_\ell$ denote the dipole moment and position of dot ℓ. Furthermore, we require the $T(t)$ to have finite support as well as causal and interpolatory properties so as to recover $\tilde{\mathbf{P}}$, $\partial_t \tilde{\mathbf{P}}$, and $\partial_t^2 \tilde{\mathbf{P}}$ at every timestep. Accordingly, we have elected to use

$$T(t) = \sum_{j=0}^{p} \lambda_j(t) \qquad (7)$$

where

$$\lambda_j(t) = \begin{cases} \frac{(1-\tau)_j}{j!} \frac{(1+\tau)_{p-j}}{(p-j)!} & j - 1 \le \tau < j \\ 0 & \text{otherwise,} \end{cases} \qquad (8)$$

$(a)_k \equiv \Gamma(a+k)/\Gamma(a)$ denotes the Pochhammer rising factorial, and $\tau \equiv t/\Delta t$. Such a $T(t)$ consists of shifted, backwards-looking Lagrange polynomials of order p (we require $p \ge 3$ to recover a twice-differentiable function), forming a temporal basis set with functions similar to the one shown in fig. 1. These functions reliably interpolate smooth functions with controllable error and have a long history of use in studies of radiative systems [26, 27].

Combining eqs. (5) and (6) and projecting the resulting field onto the spatiotemporal basis functions produces a marching-on-in-time system of the form

$$\mathcal{L}^{(m)} + \sum_{k=0}^{m} \mathcal{Z}^{(k)} \mathcal{A}^{(m-k)} = \mathcal{F}^{(m)}. \qquad (9)$$

In this (block $N_s \times N_s$) matrix equation

$$\mathcal{L}_\ell^{(m)} = \langle \mathbf{S}_\ell(\mathbf{r}), \tilde{\mathbf{E}}_L(\mathbf{r}, m\,\Delta t) \rangle \qquad (10\text{a})$$

$$\mathcal{Z}_{\ell\ell'}^{(k)} = \langle \mathbf{S}_\ell(\mathbf{r}), \tilde{\mathfrak{F}}\{\mathbf{S}_{\ell'}(\mathbf{r}) T(k\,\Delta t)\} \rangle \qquad (10\text{b})$$

$$\mathcal{F}_\ell^{(m)} = \langle \mathbf{S}_\ell(\mathbf{r}), \tilde{\mathbf{E}}(\mathbf{r}, m\,\Delta t) \rangle \qquad (10\text{c})$$

where $\langle \cdot, \cdot \rangle$ denotes the scalar product of two functions. As we have elected to use a uniform Δt, the summation in eq. (9) represents a discrete convolution that will produce $\mathcal{F}^{(m)}$ given only $\mathcal{A}^{(m' \le m)}$. To link $\mathcal{A}^{(m)}$ with the density matrix in eq. (4), we take

$$\mathcal{A}_\ell^{(m)} \equiv \tilde{\rho}_{\ell,01}(t = m\,\Delta t) \qquad (11)$$

as the off-diagonal matrix elements (coherences) of $\tilde{\rho}_\ell$ directly characterize the dipole radiating at $\mathbf{r}_\ell$ under the rotating-wave approximation. Consequently, determining $\mathcal{A}^{(m+1)}$ amounts to integrating eq. (4) from $t_i = m\,\Delta t$ to $t_f = (m+1)\,\Delta t$ for every quantum dot in the system. For this, we make use of the predictor/corrector scheme detailed in [28]. Defining $t_m \equiv m\,\Delta t$ and approximating $\tilde{\rho}(t)$ as a weighted sum of complex exponentials, the predictor/corrector scheme proceeds with an extrapolation predictor step,

$$\tilde{\rho}_\ell(t_{m+1}) \leftarrow \sum_{w=0}^{W-1} \mathcal{P}_w^{(0)} \tilde{\rho}_\ell(t_{m-w}) + \mathcal{P}_w^{(1)} \partial_t \tilde{\rho}_\ell(t_{m-w}), \quad (12)$$

and iterated corrector steps,

$$\tilde{\rho}_\ell(t_{m+1}) \leftarrow \sum_{w=-1}^{W-1} \mathcal{C}_w^{(0)} \tilde{\rho}_\ell(t_{m-w}) + \mathcal{C}_w^{(1)} \partial_t \tilde{\rho}_\ell(t_{m-w}) \quad (13)$$

($\mathcal{C}_{-1}^{(0)} \equiv 0$ by construction) to advance the system by Δt. Such an integrator has significantly better convergence properties than Runge-Kutta integrators for equations of the type seen in eq. (4).

To summarize, one timestep of our solution strategy proceeds as follows:

1. At timestep m, use eqs. (11) and (12) to predict $\mathcal{A}^{(m+1)}$. This prediction depends only on the known history of the system and does not require the calculation of any electromagnetic interactions.

2. Use eq. (9) to calculate $\mathcal{F}^{(m+1)}$. Having extrapolated $\mathcal{A}^{(m+1)}$ in step 1, $\mathcal{F}^{(m+1)}$ will contain information from quantum dots within $c\,\Delta t$ of each other.

3. Produce $\partial_t \tilde{\rho}(t_{m+1})$ (and thus $\partial_t \mathcal{A}^{(m+1)}$) by evaluating eq. (4) with the $\mathcal{F}^{(m+1)}$ found in step 2.

4. Correct $\mathcal{A}^{(m+1)}$ with eq. (13) and $\partial_t \mathcal{A}^{(m+1)}$ found in step 3. Repeat steps 2 through 4 until $\mathcal{A}^{(m+1)}$ has sufficiently converged, then set $m \leftarrow m + 1$.

Quantity	Symbol	Value
Speed of light	c	$300\,\mu\mathrm{m}\,\mathrm{ps}^{-1}$
Transition frequency	ω_0	$1500\,\mathrm{meV}/\hbar$
Transition dipole moment	$\mathbf{d}$	$10\,e\,a_0$ (uniform)
Decoherence times	T_1, T_2	10 ps and 20 ps
Laser frequency	ω_L	$1500\,\mathrm{meV}/\hbar$
Laser wavevector	$\mathbf{k}_L$	ω_L/c ($\mathbf{k}_L \cdot \mathbf{d} = 0$)
Pulse width	σ/ω_L	1 ps
Pulse area	–	π

TABLE I. Simulation parameters (unless otherwise stated); e and a_0 denote the elementary charge and Bohr radius. The decoherence times here, while shorter than those typical of optical resonance experiments, afford a shorter computational time but preserve dynamical emission phenomena.

IV. NUMERICAL RESULTS

Here we detail the results of investigations into coupled quantum dot behavior with the model presented thus far. Our algorithm reliably handles tens of thousands of quantum dots and can simulate ten picoseconds of system dynamics in two days on a single processor. We perform simulations of systems of quantum dots randomly distributed throughout a simulation volume experiencing a laser pulse of the form

$$\tilde{\mathbf{E}}_L(\mathbf{r}, t) = \tilde{\mathbf{E}}_0 e^{-(\mathbf{k}_L \cdot \mathbf{r} - \omega_L t)^2/(2\sigma^2)}. \qquad (14)$$

Table I provides the physical system parameters unless otherwise stated.

A. Stability & adjacency effects

Figure 2 details $\rho_{00}(t)$ for two-, and 1024-particle simulations shown against a solution of eq. (4) for a quantum dot evolving according to $\tilde{\mathbf{E}}_L(\mathbf{r}, t)$ alone. The system in fig. 2(a) contains two quantum dots with a separation of 6.3 nm perpendicular to their mutual $\mathbf{d}$ to ensure large contributions from the near-field term of eq. (5). The two quantum dots in this system follow the same trajectory and both excite far less than either would in response to the incident laser alone. These signatures indicate the effect arises as a dynamical frequency shift that brings adjacent quantum dots out of resonance with the applied electric field. We note that this suppression effect occured to varying degrees for all near-field arrangements of two quantum dots that we investigated. In fig. 2(b), the system contains the same two-dot arrangement as in (a), however we have added an additional 1024 quantum dots randomly distributed throughout a $6.4 \times 10^{-2}\,\mu\mathrm{m}^3$ cube centered around the original pair. Most of these additional quantum dot populations deviate little from those produced by the laser-only pulse due to the large separation between particles. Nevertheless, as we have filled the cube randomly, some regions of the system contain localized clusters of quantum dots that produce the
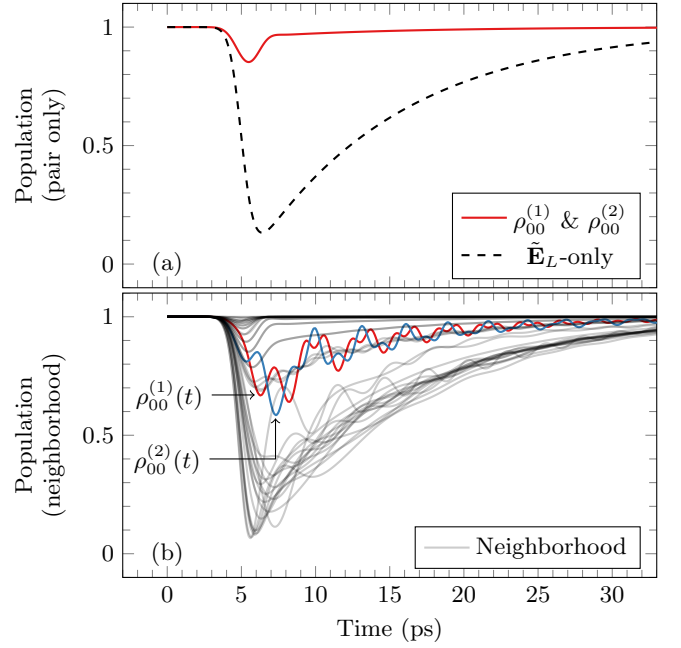

FIG. 2. Population dynamics of adjacent quantum dots (top, shown with the trajectory of a quantum dot driven exclusively by the external laser in black) and a 1024-particle neighborhood (dots (1) and (2) maintain their separation and orientation between simulations). The interaction between particles gives a greatly diminished response to the external pulse through a dynamical detuning of the two-dot system. The majority of the neighboring particles in the 1024-dot system follow trajectories nearly identical to that prescribed by the laser (omitted for clarity); many-dot effects, however, produce significant oscillatory modes in the evolution of selected quantum dots (shown in gray). Note that $\rho_{00}^{(1)}$ and $\rho_{00}^{(2)}$ appear to have *two* coherent modes in the presence of multiple dots: a high-frequency oscillation between the pair, as well as a low-frequency oscillation of the group about a decaying envelope.

suppression effect detailed above (for two adjacent particles) or populations with higher frequency oscillations (in the case of clusters with three or more quantum dots). Specifically, the two "original" quantum dots acquire an out-of-phase oscillation with respect to each other as well as a lower frequency in-phase oscillation of the pair about a decaying envelope.

Figure 3 further illustrates the near-field coupling between quantum dots. Here, 1024 quantum dots randomly fill an $8 \times 10^{-3}\,\mu\mathrm{m}^3$ cube and the same 1 ps Gaussian π-pulse illuminates the system. Without any inter-dot interactions, such a pulse would perfectly transition every quantum dot from $|0\rangle$ to $|1\rangle$, leaving behind no polarization after the pulse has passed. As the system in fig. 3 has experienced most of the pulse, the majority of the quantum dots behave this way. A number of particles remain polarized well after the pulse has passed through the system, however, due to their apparent proximity.
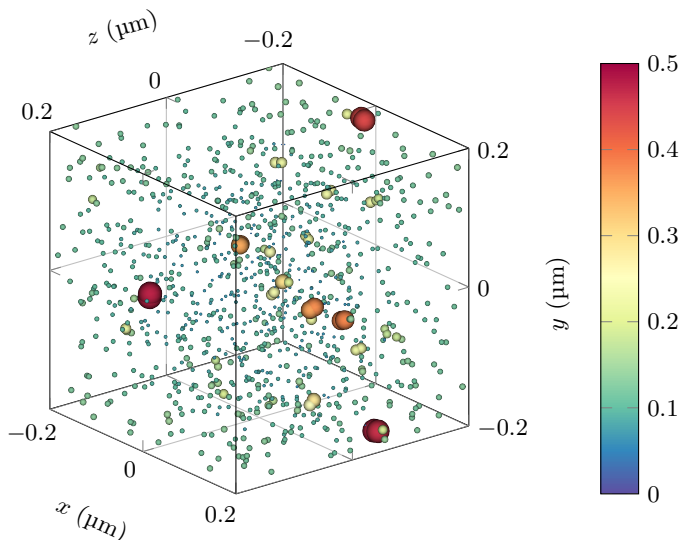
FIG. 3. Spatial distribution of $|\tilde{\rho}_{01}|$ for 1024 quantum dots as an indicator of polarization. Recorded at $t = 2$ ps relative to the peak of a 1 ps-wide π-pulse, the color and size of each sphere indicates the location of each quantum dot and its polarization. Following a π-pulse, a single quantum dot would have no remnant polarization; here, due to the near-field interactions between particles, clusters of quantum dots remain in highly-polarized states depending on their separation.
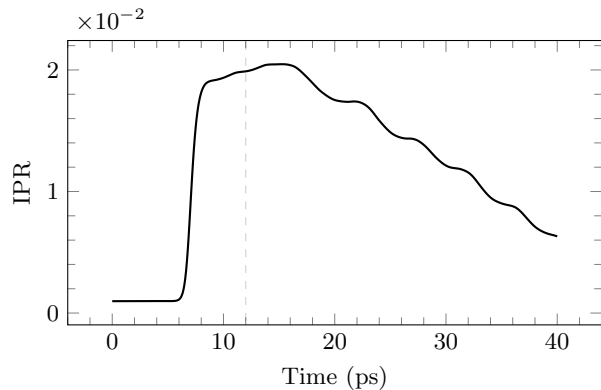

FIG. 4. Inverse participation ratio (IPR) for the system shown in fig. 3. The dashed line indicates the sample time for fig. 3.

B. Polarization enhancement

Borrowing from standard measures of localization (in which one calculates integrals of $\mathbf{E}$ over the simulation volume), we have adapted the inverse participation ratio (IPR) of the dot polarization as

$$\mathrm{IPR}(t) = \frac{\sum_\ell |\tilde{\mathbf{p}}_\ell(t)|^4}{\left(\sum_\ell |\tilde{\mathbf{p}}_\ell(t)|^2\right)^2} \qquad (15)$$

to provide a quantitative description of these phenomena [29]. Figure 4 shows this quantity for the system in

fig. 3. The maximum IPR occurs some time after the pulse has passed through the system, indicating strongly-coupled quantum dots retain their polarization longer than their neighbors. Moreover, this dynamical localization effect features oscillations which suggests many-dot effects contribute to the dynamics within a narrow spectral region.

Figure 5 depicts the evolution of $|\rho_{01}(\mathbf{r})|$ as an indicator of $\tilde{\mathbf{P}}$ for a cylinder containing 10 000 quantum dots. The cylinder has a radius of 0.2 μm and a length of 4 μm, and the incident $\mathbf{k}_L$ lies along the cylindrical axis (again perpendicular to $\mathbf{d}$ so as to maximize the long-distance interaction between quantum dots). This simulation captures the suppression effects of figs. 2 and 3 as a small number of quantum dots remain in an unexcited state while the cylinder polarizes around them. Additionally, due to the length of the cylinder, larger regions of enhanced polarization begin to appear as the system polarizes—an effect we did not observe in sub-wavelength structures. We liken these nodes to standing waves in a cavity that arise from the far-field interaction term of eq. (5). As the pulse varies little over the length of the cylinder, identical simulations run without interactions (i.e. $\mathcal{Z} = 0$ everywhere) produce homogeneous polarization distributions. Reducing the simulation to a planar geometry (fig. 6) preserves both the short-range (dark, adjacent quantum dots) and long-range (regions of enhanced/diminished polarization) phenomena observed in fig. 5. We note these geometries produce a much weaker effect than their fully three dimensional counterparts, though larger simulations with greater far-field contributions or quantum dots engineered to have a larger dipole moment may produce more measurable effects.

C. Inhomogeneous broadening

Thusfar we have investigated only homogeneous systems (i.e. an identical ω_0 for every quantum dot in the system). To probe the effects of interaction-independent inhomogeneities (possibly occurring due to some experimental variation in quantum dot sizes), fig. 7 presents four simulations with normally-distributed transition frequencies characterized by a width parameter. In simulations with mild detuning, we observe a distribution pattern characteristic of the enhancement phenomenon seen in fig. 5. More variation in the detuning distribution, however, quickly serves to destroy these phenomena leaving only "pulse-driven" effects. At present, inhomogeneous broadening in quantum dots typically exceeds the values used in fig. 7. Impurity-bound excitons have greatly diminished inhomogeneous effects and thus could offer an avenue to observe these phenomena [30].
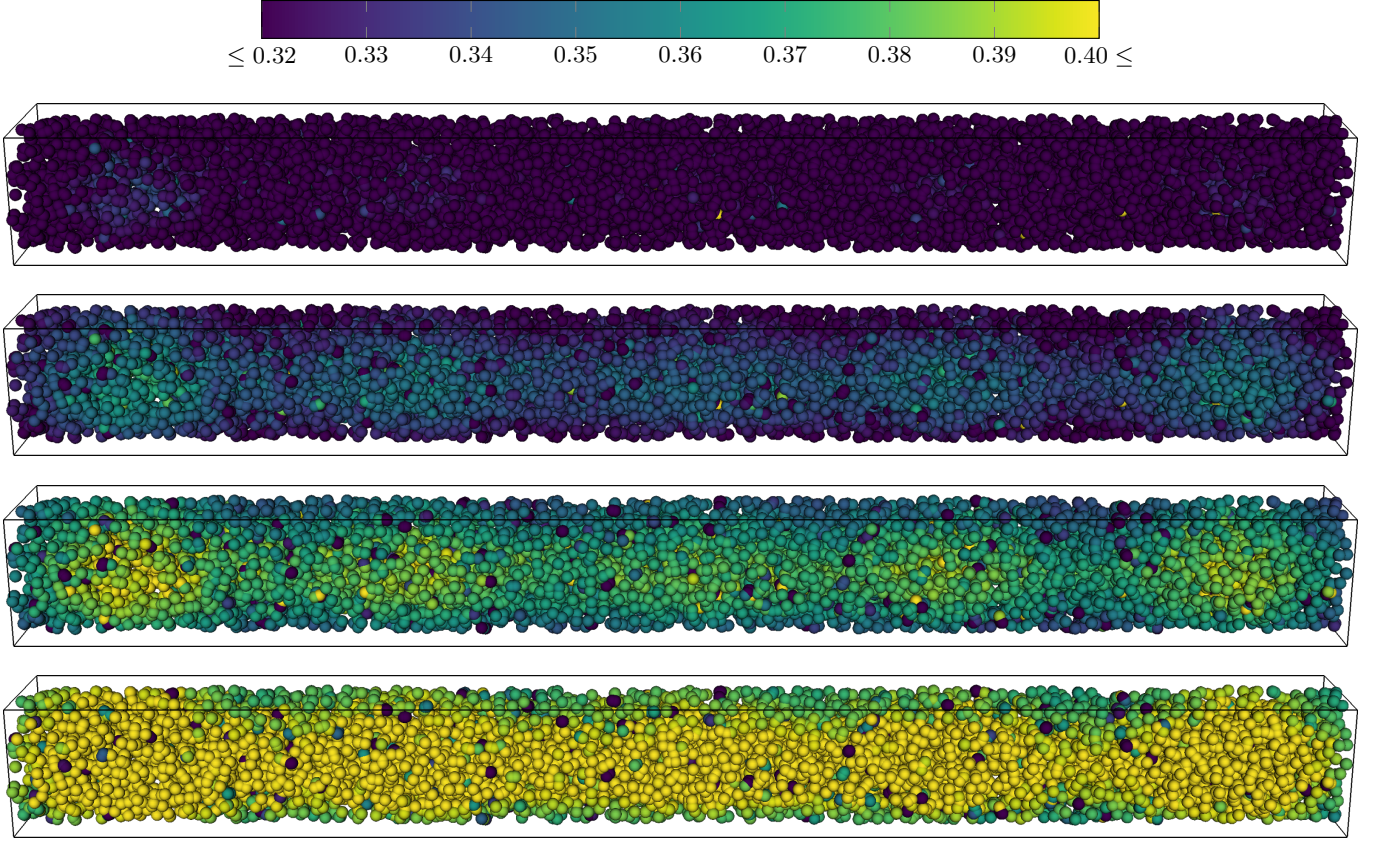
FIG. 5. Coloration of $|\tilde{\rho}_{01}|$ at $t_1 = -0.05\,\mathrm{ps}$, $t_2 = 0\,\mathrm{ps}$, $t_3 = 0.05\,\mathrm{ps}$, and $t_4 = 0.10\,\mathrm{ps}$ relative to the peak of a $1\,\mathrm{ps}$-wide pulse. $10\,000$ quantum dots randomly distributed throughout a $0.2\,\mu\mathrm{m}$ (radius) $\times\,4\,\mu\mathrm{m}$ cylinder oriented along $\mathbf{k}_L$ demonstrate near-field the effects of fig. 2 as distinct, outlying bright/dark quantum dots. Additionally, the size of the system allows for wavelength-scale phenomena that appear here as five standing regions of enhanced polarization. (Note that we model quantum dots as point objects; the size of the spheres here has no physical interpretation.)
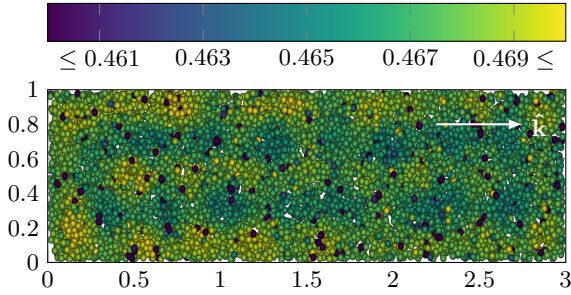

FIG. 6. Coloration of $|\tilde{\rho}_{01}|$ for $10\,000$ quantum dots arranged in a finite planar geometry (in units of λ). The slab displays a prominent polarization pattern $1.25\,\mathrm{ps}$ after the peak of a $1\,\mathrm{ps}$ pulse.

V. CONCLUSIONS & FUTURE WORK

Here we developed a robust, fine-grained algorithm to solve for the dynamics of an ensemble of quantum dots that couple in response to external light fields. By making use of an integral equation kernel to propagate radiated fields, our model facilitates simulations of thousands of quantum dots in three dimensions with accurate bookkeeping of both near and far radiation fields. Our simulations predict a suppression effect between adjacent quantum dots that screens out the incident laser pulse and we interpret this effect as a dynamical detuning that shifts the effective ω_0 of the affected quantum dots. Moreover, we observe additional oscillatory behavior and localization effects in larger clusters of particles. These effects could prove useful to identify optically quantum dot "molecules" in an extended sample by detecting residual localized polarization following integral π pulse(s)—we expect that an experimental π-pulse calibrated to a single quantum dot with a scanning-type polarization measurement [6] would reveal signatures of these effects in dense samples. Finally, in larger systems of densely-packed quantum dots, we see significant localization that present as regions of enhanced polarization over length scales comparable to that of the incident wavelength. These effects persist in simulations with other extended geometries and in simulations with inhomogeneously-broadened transition frequencies, though the effects quickly disappear with
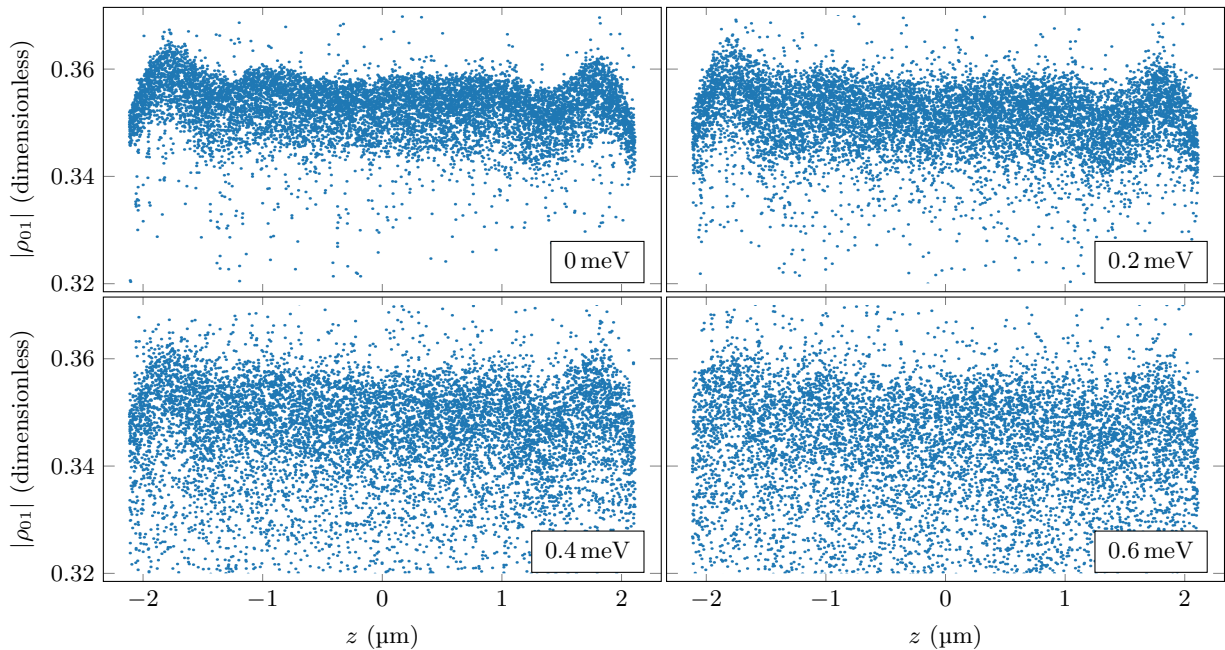
FIG. 7. z-distribution of polarization $|\tilde{\rho}_{01}|$ for the geometry in fig. 5. In each simulation, 10 000 quantum dots had random Gaussian noise (with width parameters of 0.0 meV, 0.2 meV, 0.4 meV and 0.6 meV) added to a resonant $\hbar\omega_0 = 1500$ meV. The induced long-range patterns in the polarization remain for mild detunings $\lesssim 0.5$ meV but have completely washed out at 0.6 meV. Additionally, each simulation displayed the characteristic near-field coupling effects of fig. 2 (not visible here).

only a few meV detuning.

Semi-classical approaches can describe some superradiant effects within a continuum formulation [7, 31, 32]. First predicted in 2005 [33] and observed in 2007 [34], superradiant effects in quantum dot ensembles have since spurred theoretical analyses into cooperative radiation mechanisms [35, 36]. While our semiclassical approach accounts for collective effects due to the secondary field emission from quantum dots, we do so in the Hamiltonian term on the right hand side of eq. (1) and not in the $\hat{\mathcal{D}}[\hat{\rho}]$ dissipator. In future work, we plan to extend our microscopic approach to include collective dissipation effects so as to better model superradiant phenomena. We expect that our approach—when extended to systems containing a larger number of quantum dots—will aid in investigating the role of many-dot interactions in systems such as nanolasers [37] that exploit these phenomena. Unfortu-

nately, the naïve $\mathcal{O}(N_s^2)$ interaction calculation presented here hampers attempts to extend these calculations to systems with $N_s \gg 10^4$. Our ongoing research includes the development of accelerated computational techniques that exploit the structure of $\mathcal{Z}$ to reduce the big-$\mathcal{O}$ complexity of eq. (9). Additionally, the technique presented here readily extends to model atomic, molecular, and semiconductor systems with richer structure (e.g. systems with energy degeneracies or biexcitonic transitions).

ACKNOWLEDGMENTS

[1] T. H. Stievater, X. Li, D. G. Steel, D. Gammon, D. S. Katzer, D. Park, C. Piermarocchi, and L. J. Sham, Phys. Rev. Lett. **87**, 133603 (2001).

[2] H. Kamada, H. Gotoh, J. Temmyo, T. Takagahara, and H. Ando, Phys. Rev. Lett. **87**, 246401 (2001).

[3] H. Htoon, T. Takagahara, D. Kulik, O. Baklenov, A. L. Holmes, and C. K. Shih, Phys. Rev. Lett. **88**, 087401 (2002).

[4] G. Y. Slepyan, S. A. Maksimenko, A. Hoffmann, and D. Bimberg, Phys. Rev. A **66**, 063804 (2002).

[5] G. Y. Slepyan, A. Magyarov, S. A. Maksimenko, A. Hoffmann, and D. Bimberg, Phys. Rev. B **70**, 045320 (2004).

[6] K. Asakura, Y. Mitsumori, H. Kosaka, K. Edamatsu, K. Akahane, N. Yamamoto, M. Sasaki, and N. Ohtani, Phys. Rev. B **87**, 241301 (2013).

[7] M. Gross and S. Haroche, Physics Reports **93**, 301 (1982).

[8] D. C. Burnham and R. Y. Chiao, Phys. Rev. **188**, 667 (1969).

[9] J. C. MacGillivray and M. S. Feld, Phys. Rev. A **14**, 1169 (1976).

[10] F. Haake, H. King, G. Schröder, J. Haus, and R. Glauber, Phys. Rev. A **20**, 2047 (1979).

[11] N. E. Rehler and J. H. Eberly, Phys. Rev. A **3**, 1735 (1971).

[12] C. R. Stroud, J. H. Eberly, W. L. Lama, and L. Mandel, Phys. Rev. A **5**, 1094 (1972).

[13] C. Vanneste and P. Sebbah, Phys. Rev. Lett. **87**, 183903 (2001).

[14] A. Fratalocchi, C. Conti, and G. Ruocco, Optics express **16**, 8342 (2008).

[15] N. Bachelard, R. Carminati, P. Sebbah, and C. Vanneste, Phys. Rev. A **91**, 043810 (2015).

[16] B. Shanker, A. A. Ergin, K. Aygun, and E. Michielssen, IEEE Transactions on Antennas and Propagation **48**, 1064 (2000).

[17] A. J. Pray, N. V. Nair, and B. Shanker, IEEE Transactions on Antennas and Propagation **60**, 3772 (2012).

[18] A. J. Pray, Y. Beghein, N. V. Nair, K. Cools, H. Bac, and B. Shanker, IEEE Transactions on Antennas and Propagation **62**, 6183 (2014).

[19] A. A. Ergin, B. Shanker, and E. Michielssen, The Journal of the Acoustical Society of America **106**, 2396 (1999), http://dx.doi.org/10.1121/1.428076.

[20] A. A. Ergin, B. Shanker, and E. Michielssen, The Journal of the Acoustical Society of America **106**, 2195 (1999), http://dx.doi.org/10.1121/1.427446.

[21] C. Glosser, C. Piermarocchi, J. Li, D. Dault, and B. Shanker, Phys. Rev. E **93**, 013305 (2016).

[22] C. Glosser, "cglosser/QuEST: v0.1.0," (2017).

[23] L. Landau and E. Lifshitz, *The Classical Theory of Fields*, Course of Theoretical Physics, Vol. 2 (Elsevier Science, 2013).

[24] C. Cohen-Tannoudji, J. Dupont-Roc, and G. Grynberg, *Photons and atoms: introduction to quantum electrodynamics* (Wiley Online Library, 1989).

[25] L. Allen and J. Eberly, *Optical Resonance and Two-level Atoms*, Dover books on physics and chemistry (Dover, 1975).

[26] G. Manara, A. Monorchio, and R. Reggiannini, IEEE Transactions on Antennas and Propagation **45**, 527 (1997).

[27] M. J. Bluck and S. P. Walker, IEEE Transactions on Antennas and Propagation **45**, 894 (1997).

[28] A. Glaser and V. Rokhlin, Journal of Scientific Computing **38**, 368 (2009).

[29] T. Schwartz, G. Bartal, S. Fishman, and M. Segev, Nature **446**, 52 (2007).

[30] M. Thewalt, Canadian Journal of Physics **55**, 1463 (1977).

[31] R. Bonifacio, P. Schwendimann, and F. Haake, Phys. Rev. A **4**, 302 (1971).

[32] R. Bonifacio, P. Schwendimann, and F. Haake, Phys. Rev. A **4**, 854 (1971).

[33] V. V. Temnov and U. Woggon, Phys. Rev. Lett. **95**, 243602 (2005).

[34] M. Scheibner, T. Schmidt, L. Worschech, A. Forchel, G. Bacher, T. Passow, and D. Hommel, Nat Phys **3**, 106 (2007).

[35] V. V. Temnov and U. Woggon, Optics express **17**, 5774 (2009).

[36] Q.-H. Chen, Y.-Y. Zhang, T. Liu, and K.-L. Wang, Phys. Rev. A **78**, 051801 (2008).

[37] F. Jahnke, C. Gies, M. Aßmann, M. Bayer, H. Leymann, A. Foerster, J. Wiersig, C. Schneider, M. Kamp, and S. Höfling, Nature communications **7** (2016).

[38] G. Guennebaud, B. Jacob, *et al.*, "Eigen v3," http://eigen.tuxfamily.org (2010).

[39] H. Childs, E. Brugger, B. Whitlock, J. Meredith, S. Ahern, D. Pugmire, K. Biagas, M. Miller, C. Harrison, G. H. Weber, H. Krishnan, T. Fogal, A. Sanderson, C. Garth, E. W. Bethel, D. Camp, O. Rübel, M. Durant, J. M. Favre, and P. Navrátil, in *High Performance Visualization–Enabling Extreme-Scale Scientific Insight* (2012) pp. 357–372.

[40] S. v. d. Walt, S. C. Colbert, and G. Varoquaux, Computing in Science and Engg. **13**, 22 (2011).

[41] E. Jones, T. Oliphant, P. Peterson, *et al.*, "SciPy: Open source scientific tools for Python," (2001–), [Online].